

Effects of Phonon Confinement on Anomalous Thermalization, Energy Transfer, and Upconversion in Ln^{3+} -Doped Gd_2O_3 Nanotubes

By Andreia G. Macedo, Rute A. S. Ferreira, Duarte Ananias, Mário S. Reis, Vitor S. Amaral, Luís D. Carlos,* and João Rocha

There is a growing interest in understanding how size-dependent quantum confinement affects the photoluminescence efficiency, excited-state dynamics, energy-transfer and thermalization phenomena in nanophosphors. For lanthanide (Ln^{3+})-doped nanocrystals, despite the localized 4f states, confinement effects are induced mostly via electron–phonon interactions. In particular, the anomalous thermalization reported so far for a handful of Ln^{3+} -doped nanocrystals has been rationalized by the absence of low-frequency phonon modes. This nanoconfinement may further impact on the Ln^{3+} luminescence dynamics, such as phonon-assisted energy transfer or upconversion processes. Here, intriguing and unprecedented anomalous thermalization in $\text{Gd}_2\text{O}_3:\text{Eu}^{3+}$ and $\text{Gd}_2\text{O}_3:\text{Yb}^{3+},\text{Er}^{3+}$ nanotubes, exhibiting up to one order of magnitude larger than previously reported for similar materials, is reported. This anomalous thermalization induces unexpected energy transfer from $\text{Eu}^{3+} \text{ } ^5\text{D}_1$ to S_6 crystallographic sites, at 11 K, and $^2\text{H}_{11/2} \rightarrow ^4\text{I}_{15/2} \text{Er}^{3+}$ upconversion emission; it is interpreted on the basis of the discretization of the phonon density of states, easily tuned by varying the annealing temperature (923–1123 K) in the synthesis procedure, and/or the Ln^{3+} concentration (0.16–6.60%).

$\text{Gd}_2\text{O}_3:\text{Yb}^{3+},\text{Er}^{3+}$ nanorods have received considerable attention^[5–14] because they exhibit shape-specific and quantum-size effects.^[14–30]

Size-dependent quantum confinement has important effects on the radiative and nonradiative electronic transitions in nanoparticles, and tuning the particles structure at the nanometer scale may result in novel optical properties for applications in 3D displays,^[31–32] light-emitting devices,^[33] and bioassays.^[34,35] Due to the confinement effect in Ln^{3+} -nanocrystals, the phonon density of states (PDOS) becomes discrete, with a cut-off on the low-energy side.^[27–30] Because the low-frequency phonons contribute most effectively to the nonradiative relaxation between closely spaced Stark levels, the lack of these low-frequency modes considerably modifies the Ln^{3+} emission dynamics, relative to that of bulk materials.

Up to now, anomalous thermalization due to the absence of low-frequency phonon modes (nanoconfinement effects) has been reported only for a few Ln^{3+} -nanocrystals.^[14,23,26–30] In 1998 Tissue et al. noticed the presence of broad $^7\text{F}_1 \rightarrow ^5\text{D}_1$ hot bands in the excitation spectra of 4–6 nm Eu_2O_3 particles at 12 K. A large increase in the intensity of these hot bands, relative to the normal excitation lines, was measured for particle sizes from 12 nm down to 4 nm.^[23] Later, Liu et al. reported hot bands of the $^4\text{I}_{15/2} \rightarrow ^4\text{F}_{7/2}$ transition (with energies up to 200 cm^{-1} higher than the energy of the zero-phonon line) in the excitation spectra of $\text{Y}_2\text{O}_3:\text{Er}^{3+}$ nanocrystals (20–40 nm) below 7 K.^[27,28] The direct phonon relaxation between the Stark levels of the $^4\text{I}_{15/2}$ ground term is restricted due to the lack of low-energy modes, and consequently, the intensity of the hot bands originating from the upper $^4\text{I}_{15/2}$ crystal field levels increases suddenly as temperature decreases below 7 K.^[27–29] This interpretation was extended to the above-mentioned anomalous hot bands in Eu_2O_3 particles.^[30] Recently, Mercier et al.^[26] and Liu et al.^[14] provided experimental evidence of anomalous thermalization in $\text{Gd}_2\text{O}_3:\text{Eu}^{3+}$ nanoparticles and $\text{Gd}_2\text{O}_3:\text{Eu}^{3+}$ nanotubes, respectively. Hot bands originating from the lowest $^7\text{F}_1$ Stark level, with an energy of 217 cm^{-1} , were observed in the excitation spectra below 50 K. Both groups interpreted this anomalous

1. Introduction

Lanthanide-containing compounds have been extensively utilized as high-performance phosphors in various devices based on the electronic, optical, and chemical properties arising from 4f electrons.^[1–4] Ln^{3+} -hydroxide and oxide ($\text{Ln} = \text{Ce}, \text{Pr}, \text{Nd}, \text{Sm}, \text{Dy}, \text{Tb}, \text{Gd}, \text{Yb}, \text{Er}$) nanocrystals, $\text{Y}_2\text{O}_3:\text{Eu}^{3+}/\text{Y}_2\text{O}_3$ core-shell composites, $\text{Y}_2\text{O}_3:\text{Eu}^{3+}$ and $\text{Gd}_2\text{O}_3:\text{Eu}^{3+}$ nanotubes, and

[*] Prof. L. D. Carlos, A. G. Macedo, Dr. R. A. S. Ferreira, Dr. M. S. Reis, Prof. V. S. Amaral
Department of Physics and CICECO
Universidade de Aveiro
3810-193 Aveiro (Portugal)
E-mail: lcarlos@ua.pt
Dr. D. Ananias, Prof. J. Rocha
Department of Chemistry and CICECO
Universidade de Aveiro
3810-193 Aveiro (Portugal)

DOI: 10.1002/adfm.200901772

thermalization effect in terms of phonon confinement. In 2003, Liu et al. suggested that the phonon-confinement effects in Ln^{3+} -containing nanocrystals may further impact on the phonon-assisted energy transfer and upconversion processes.^[28]

Herein, we will describe the photoluminescence features of Eu^{3+} in Gd_2O_3 nanotubes (0.16%, 1.00%, 3.30%, and 6.60% Eu^{3+} molar content) and nanorods (3.30%) and of Er^{3+} in Yb^{3+} , Er^{3+} co-doped Gd_2O_3 nanotubes (5.00% Yb^{3+} , 1.20% Er^{3+} molar content) synthesized using different annealing conditions. The nanotubes exhibit a remarkable anomalous thermalization effect, one order of magnitude larger than that previously reported for similar $\text{Gd}_2\text{O}_3:\text{Eu}^{3+}$ (3.96%) nanotubes,^[14] which strongly depends on the thermal history and Ln^{3+} content. At 11 K, the $\text{Gd}_2\text{O}_3:\text{Eu}^{3+}$ nanotubes display a unique energy transfer from Eu^{3+} C_2 to S_6 crystallographic sites, while the Gd_2O_3 nanotubes co-doped with Yb^{3+} , Er^{3+} exhibit the unexpected $^2\text{H}_{11/2} \rightarrow ^5\text{I}_{15/2}$ upconversion green emission.

This paper is organized in the following way:

- We start by presenting the structural and magnetic data of $\text{Gd}_2\text{O}_3:\text{Eu}^{3+}$ and $\text{Gd}_2\text{O}_3:\text{Yb}^{3+}, \text{Er}^{3+}$ nanotubes (with the C_2 and S_6 crystallographic Ln^{3+} sites), and its emission and excitation features as a function of temperature (11–300 K). For the $\text{Gd}_2\text{O}_3:\text{Eu}^{3+}$ nanotubes, the influence of the morphology and annealing conditions on the absolute quantum yields and the $\text{Eu}^{3+}(S_6)$ -to- $\text{Eu}^{3+}(C_2)$ and Gd_2O_3 -to- Eu^{3+} (both C_2 and S_6) energy-transfer rates are also addressed.
- Secondly, the temperature-dependence of the intensity of the $^7\text{F}_1 \rightarrow ^5\text{D}_1$ and $^2\text{H}_{11/2} \rightarrow ^5\text{I}_{15/2}$ transitions is studied as a function of the annealing conditions and Eu^{3+} or $\text{Yb}^{3+}, \text{Er}^{3+}$ content.
- Finally, we demonstrate that this anomalous thermalization effect induces the unexpected presence at 11 K of both, $\text{Eu}^{3+}(C_2) \rightarrow \text{Eu}^{3+}(S_6)$ energy transfer ($\text{Gd}_2\text{O}_3:\text{Eu}^{3+}$) and $^2\text{H}_{11/2} \rightarrow ^5\text{I}_{15/2}$ upconversion emission ($\text{Gd}_2\text{O}_3:\text{Yb}^{3+}, \text{Er}^{3+}$), and that this phenomena could be rationalized on the basis of the size-dependent discretization of the PDOS.

2. Results and Discussion

2.1. Structural and Magnetic Characterization

Transmission electron microscopy (TEM) images (Fig. 1A,B) show regular cylindrical $\text{Gd}_2\text{O}_3:\text{Eu}^{3+}$ nanotubes of 100–180 nm in length (some even longer) and diameters of 5–25 nm (Fig. S1 of Supporting Information (SI)). The structure is cubic, as shown by the electron diffraction pattern (inset in Fig. 1A). The mean length and diameter (Fig. S1 (SI)), of the $\text{Gd}_2\text{O}_3:\text{Eu}^{3+}$ nanorods shown in Figure 1C are much less well defined, but tend to be larger than those of the nanotubes in Figure 1A and 1B. The nanotubes are polycrystalline, as revealed by the dark-field and high-resolution (HR) TEM images (Fig. 1D,E), with nanocrystallites of lateral dimensions of ca. 10 nm; using powder X-ray diffraction (XRD) data and the Scherrer equation, it was found that all nanotubes studied have similar sizes (Fig. S2 (SI)). The thickness of the nanotubes wall is 5–10 nm. The morphology of the $\text{Gd}_2\text{O}_3:\text{Yb}^{3+}, \text{Er}^{3+}$ nanotubes is similar.

Powder XRD patterns of the as-prepared $\text{Gd}_2\text{O}_3:\text{Ln}^{3+}$ ($\text{Ln} = \text{Eu}$ or Er/Yb) samples were indexed to a pure hexagonal $\text{Gd}(\text{OH})_3$ structure (Powder diffraction file (PDF): 83-2037), while the patterns of the annealed samples are characteristic of the Gd_2O_3 cubic phase^[36] (Fig. S2A,B (SI)). The cubic cell lattice parameter (a) is 10.819 (nanotubes), 10.816 (nanorods), and 10.816 (microcrystals) Å. No lattice parameter change was observed for different annealing conditions and aging times (Fig. S2C (SI)). Considering the first coordination sphere of Gd^{3+} , the gadolinium oxide has a bixbyite structure $Ia\bar{3}$ with two crystallographically unique cation sites, exhibiting C_2 (noncentrosymmetric) and S_6 (centrosymmetric) local symmetry in a 3:1 population ratio. Minor interstitial sites may occur.^[37]

Although the crystalline structure exhibits the same phase transitions under annealing, the thermogravimetry curves of nanocrystals and microcrystals exhibit some differences (Fig. S3 (SI)). Approximately 8% weight loss is observed in the range of 599–635 K, when the $\text{Gd}(\text{OH})_3$ hexagonal structure loses one water molecule and rearranges to a monoclinic phase, $\text{Gd}(\text{OH})_3 \rightarrow \text{Gd}(\text{OOH}) + \text{H}_2\text{O}$.^[38–39]

Another mass loss is observed between 723 and 843 K. At this stage, hydroxyl, nitrate, and carbonate groups are eliminated, generating oxide (Gd_2O_3) from the hydroxide phase. For the nanocrystals (nanotubes and nanorods), complete monoclinic-to-cubic phase conversion requires temperatures up to 908 K.

DC magnetic susceptibility was measured as a function of temperature (Fig. S4 (SI)). From this result, it is possible to extract the paramagnetic effective moment $p_{\text{eff}} = g\sqrt{J(J+1)}\mu_B$ (where g , J , and μ_B represent the Landé factor, the total angular momentum, and Bohr magneton, respectively) and the paramagnetic Curie temperature θ_p . For example, the p_{eff} of the $\text{Gd}_2\text{O}_3:\text{Eu}^{3+}$ nanotubes with 3.30% and annealing at 973 K during 3 h is $7.1 \pm 1 \mu_B$, lower than the theoretical value of $7.8 \mu_B$ (considering 3.30% of nonmagnetic Eu^{3+} ions, $J=0$). Using polarized-neutron experiments to measure the temperature dependence of the susceptibility of the Gd^{3+} ions at the two different C_2 and S_6 sites in cubic Gd_2O_3 , Moon and Koehler showed the formation of antiferromagnetic clusters of $\text{Gd}^{3+}(C_2)$ ions, reducing therefore the susceptibility of these ions.^[40,41] The temperature dependence below 10 K of the magnetic susceptibility of the Gd^{3+} ions at both sites was explained considering the effects of short-range magnetic order (within those clusters) on the susceptibility of $\text{Gd}^{3+}(C_2)$ and $\text{Gd}^{3+}(S_6)$ ions. Thus, we consider cluster formation extended for a wide range of temperatures as a possible explanation for the reduction of the paramagnetic effective moment (see Ref. [40] for further details).

2.2. Photoluminescence Spectra and Emission Quantum Yields

Figure 2A compares the 11 K emission spectra of $\text{Gd}_2\text{O}_3:\text{Eu}^{3+}$ nanotubes, nanorods, and microcrystals under 274.4 nm excitation. The spectra display the $^5\text{D}_0 \rightarrow ^7\text{F}_{0-4}$ transitions of the S_6 and C_2 Eu^{3+} local environments.^[43] Apart from slight differences in the full-width-at-half maximum (fwhm) of the emission lines, the spectra of the $\text{Gd}_2\text{O}_3:\text{Eu}^{3+}$ nanorods, nanotubes, and microcrystals are identical. For instance, the fwhm of the $^5\text{D}_0 \rightarrow ^7\text{F}_{1a}$ line

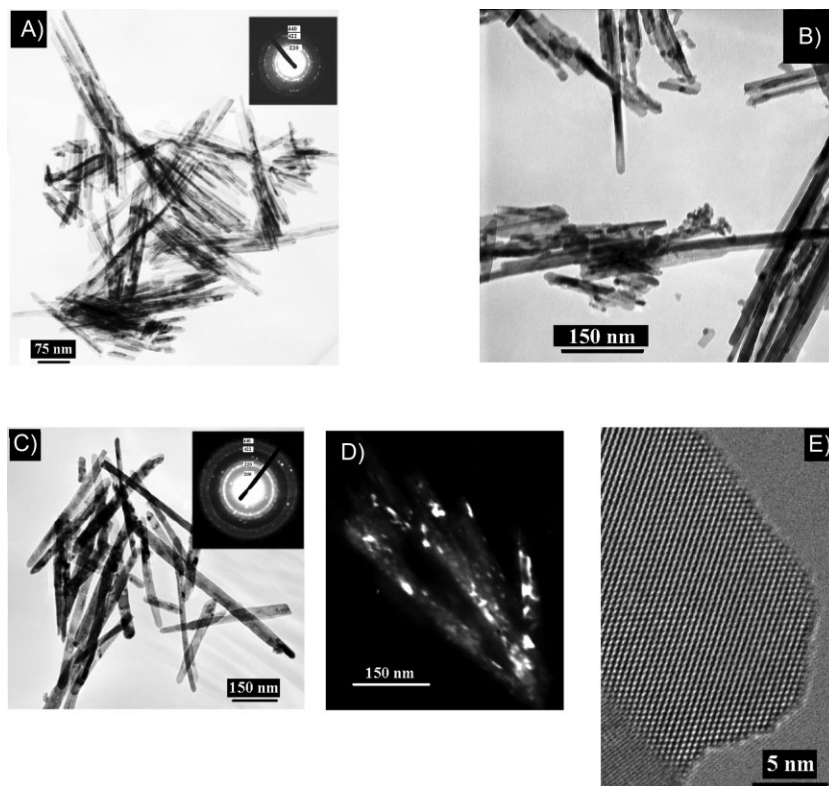


Figure 1. TEM images of $\text{Gd}_2\text{O}_3:\text{Eu}^{3+}$. A) Nanotubes (3.30%), annealed at 773 K for 1 h. B) Nanotubes (3.30%), annealed at 973 K for 3 h. C) Nanorods (3.30%), annealed at 973 K for 3 h. D) Dark-field image of nanotubes showing nanocrystallites (ca. 10 nm). E) HRTEM image of a nanocrystallite (3.30%), annealed at 973 K for 3 h.

(S_6) at 582 nm is 29.1 ± 0.4 (nanotubes), 23.3 ± 0.9 (nanorods), and 17.93 ± 0.3 (microcrystal) cm^{-1} . This broadening of the spectral lines, already reported for $\text{Er}^{3+}:\text{Y}_2\text{O}_3$ nanocrystals,^[27] is attributed to inhomogeneous broadening induced by lattice defects and/or a layer of amorphous material at the surface of the nanomaterials.

Figure 2B shows an expansion of the $^5\text{D}_0 \rightarrow ^7\text{F}_{0,1}$ spectral region for the $\text{Gd}_2\text{O}_3:\text{Eu}^{3+}$ nanotubes (0.16%, 3.30%, and 6.60%) and the assignment of the emission lines to the S_6 and C_2 local sites, based on the 523.5 and 527.6 nm excitation wavelength dependence that favours the emission from the Eu^{3+} ions at S_6 and C_2 sites, respectively. The two lines marked with asterisks in Figure 2B, already identified by Buijs et al.^[43] and Hunt et al.^[44] and also observed for the nanorods and microcrystals (not shown), are attributed to electron–phonon interaction caused from the coupling between the $^5\text{D}_0 \rightarrow ^7\text{F}_{1a}$ (C_2) and $^5\text{D}_0 \rightarrow ^7\text{F}_{1b}$ (S_6) transitions and vibrational modes. The line at 585.4 nm ($\sim 78 \text{ cm}^{-1}$) is favored by selective $\text{Eu}^{3+}(C_2)$ excitation, whereas the line at $\sim 595.6 \text{ nm}$ ($\sim 106 \text{ cm}^{-1}$) is favored by selective $\text{Eu}^{3+}(S_6)$ excitation (Fig. S5 (SI)). These two vibrational modes are observed in the Fourier transform (FT) Raman spectrum (Fig. S6 (SI)).

Figure 3 shows the excitation spectra (11 K) of the $\text{Gd}_2\text{O}_3:\text{Eu}^{3+}$ nanotubes, nanorods, and microcrystals recorded by selectively monitoring the $^5\text{D}_0 \rightarrow ^7\text{F}_2(C_2)$ and $^5\text{D}_0 \rightarrow ^7\text{F}_1(S_6)$ emissions at 611.0 and 582.4 nm, respectively. The strong broad band at $\sim 250 \text{ nm}$ is ascribed to O \rightarrow Eu ligand-to-metal charge transfer

(LMCT) transitions.^[42] Beside the Eu^{3+} intra- $4f^6$ lines, $^7\text{F}_0 \rightarrow ^5\text{D}_{0,4}$, $^5\text{L}_6$, $^5\text{G}_{2-6}$, the spectra exhibit the Gd^{3+} intra- $4f^7$ lines, $^8\text{S}_{7/2} \rightarrow ^6\text{I}_{7/2-17/2}$, $^6\text{P}_{3/2-7/2}$, showing efficient Gd^{3+} -to- Eu^{3+} energy transfer for the C_2 and S_6 sites.^[43,45] The energy difference between the maximum intensity peaks of the LMCT transitions for the two monitored wavelengths (248 and 255 nm, for S_6 and C_2 , respectively) is due to the shorter Eu–O bond length of the S_6 sites.^[36] The excitation spectra of the $\text{Eu}^{3+}:\text{Gd}_2\text{O}_3$ nanocrystals resemble that of the microcrystals although a blue-shift of the LMCT band relative to the bulk materials is observed (Fig. S7A,B (SI)). This effect has been previously discussed by Igarashi et al.: the reduction of particle size causes lattice distortion and the lattice constant to be larger; such a change of crystallinity increases the ionic character of the Eu–O bonds shifting the LMCT excitation peak towards the higher-energy side.^[46]

Based on the emission and excitation spectra at 11 K (Fig. 2B and 4A,B; Fig. S5 (SI)), the assignment of the energy levels below $30\,000 \text{ cm}^{-1}$ was performed (Scheme S1 (SI)). The energy levels of the C_2 site are similar to those reported for analogous $\text{Gd}_2\text{O}_3:\text{Eu}^{3+}$ nanotubes,^[14] nanorods,^[18,19] and microcrystals.^[43] For $\text{Eu}^{3+}(S_6)$, only the $^5\text{D}_{1a,b}$ levels can be unambiguously assigned (energies in accordance with those reported by Buijs et al.^[43]), the $^7\text{F}_0 \rightarrow ^5\text{D}_{1a,b}$ and $^5\text{D}_0 \rightarrow ^7\text{F}_{1a,b}$ transitions are the only ones allowed by the site symmetry

selection rules.

Table 1 lists the room-temperature emission quantum yield values measured for $\text{Gd}_2\text{O}_3:\text{Eu}^{3+}$ nanotubes, nanorods and microcrystals, upon excitation at 255 nm (LMCT band, intensity maximum of the excitation spectra). Among the $\text{Gd}_2\text{O}_3:\text{Eu}^{3+}$ nanocrystals, those annealed at 1023 K for 3 h display the maximum emission quantum yield values of 0.58–0.59. These values are lower than the value of the microcrystals (0.70) due to the larger surface-to-volume ratio which induces additional nonradiative depopulation paths. Changing the annealing parameters (time, temperature, or pH), induces small variations in the emission quantum yield values (Table 1).

The $^5\text{D}_0$ emission decay curves ascribed to the $\text{Eu}^{3+}(C_2)$ ions for $\text{Gd}_2\text{O}_3:\text{Eu}^{3+}$ nanotubes, nanorods, and microcrystals were monitored within the $^5\text{D}_0 \rightarrow ^7\text{F}_2$ transition at 11 and 300 K, under 394 nm excitation wavelength. All the emission decay curves are well reproduced by a single exponential function, except for the low Eu^{3+} -content (0.16% and 1.00%) nanotubes, whose decay curves display a rise time component assigned to the nonradiative energy transfer between the $^5\text{D}_1$ level of the $\text{Eu}^{3+}(S_6)$ ions and the $^5\text{D}_0$ level of the $\text{Eu}^{3+}(C_2)$ ones.^[47] The estimated lifetime values are always longer than the lifetime values of the microcrystals ($1.00 \pm 0.01 \text{ ms}$, at 11 and 300 K), indicating a small effective refraction index (or filling factor^[48]) for the nanocrystals. For instance, the $^5\text{D}_0$ lifetime values measured for $\text{Gd}_2\text{O}_3:\text{Eu}^{3+}$ nanorods and nanotubes (3.30%) calcined at 973 K during 3 h are 1.46 ± 0.01

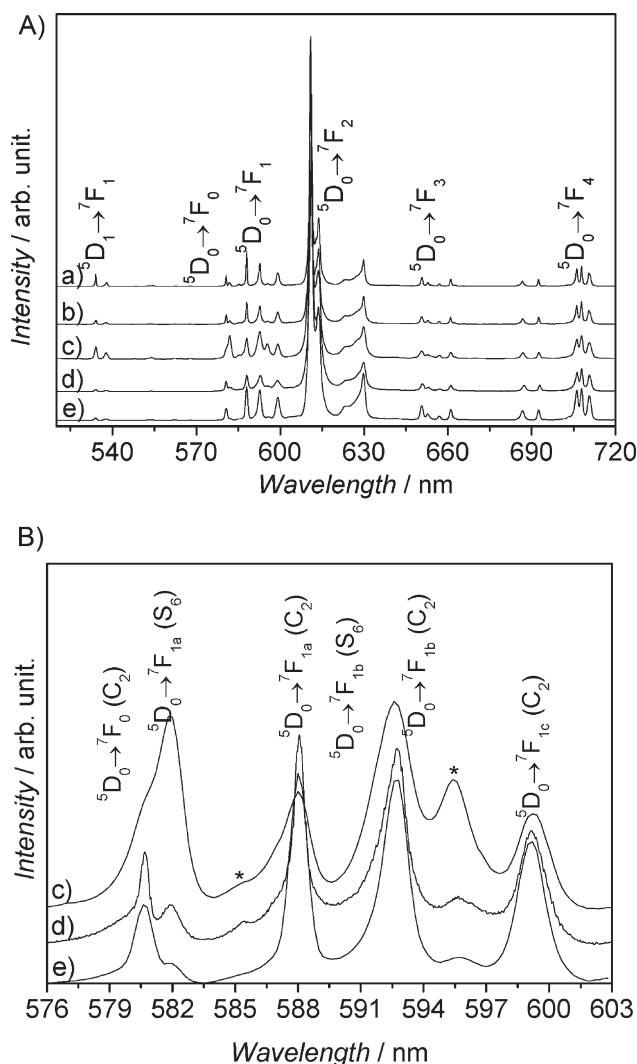


Figure 2. A) Emission spectra (11 K) of $\text{Gd}_2\text{O}_3:\text{Eu}^{3+}$ a) microcrystals (3.65%), b) nanorods (3.30%), and c–e) nanotubes containing 0.16% (c), 3.30% (d), and 6.60% (e) Eu^{3+} under 274.4 nm excitation. B) Expansion of the $^5\text{D}_0 \rightarrow ^7\text{F}_{0,1}$ transitions of $\text{Gd}_2\text{O}_3:\text{Eu}^{3+}$ nanotubes (0.16% (c), 3.30% (d), and 6.60% (e)). All samples were annealed at 973 K for 3 h.

and 1.76 ± 0.01 ms (11 K), respectively, and 1.46 ± 0.01 and 1.45 ± 0.01 ms (300 K), respectively. The values found for the nanotubes are shorter than those reported for analogous samples (Eu^{3+} content of 3.96%) by Liu et al.^[14], which were 2.19 (10 K) and 2.01 ms (295 K), due to differences in the morphology of the two samples; the nonsolid medium surrounding the nanotubes could change the effective index of refraction (or filling factor) and consequently the radiative lifetime.^[48] The filling factor, showing what fraction of the sample is occupied by the nanotubes, is estimated to be 66% for our $\text{Gd}_2\text{O}_3:\text{Eu}^{3+}$ nanotubes (55% in the sample prepared by Liu et al.^[14]).

Figure 4A,B show the excitation spectra (11 K) in the region of the $^7\text{F}_{0,1} \rightarrow ^5\text{D}_1$ transition (520–540 nm) by monitoring, respectively, the $^5\text{D}_0 \rightarrow ^7\text{F}_2$ (C_2) emission at 611.0 nm and the $^5\text{D}_0 \rightarrow ^7\text{F}_1$ (S_6) emission at 582.4 nm. The high-energy $^5\text{D}_1$ Stark component ($^5\text{D}_{1c}$) of C_2 site and the low-energy $^5\text{D}_1$ Stark component ($^5\text{D}_{1a}$) of

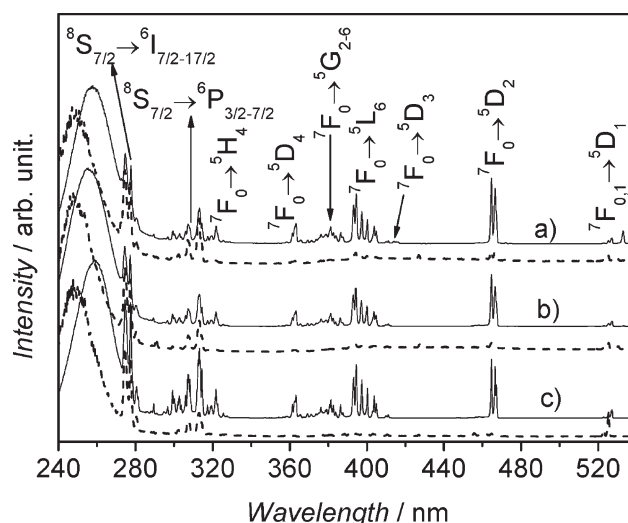


Figure 3. Excitation spectra (11 K) of $\text{Gd}_2\text{O}_3:\text{Eu}^{3+}$ a) nanotubes (3.30%), b) nanorods (3.30%), and c) microcrystals (3.65%) while monitoring the $^5\text{D}_0 \rightarrow ^7\text{F}_2$ emission (C_2) at 611 nm (solid line) and the $^5\text{D}_0 \rightarrow ^7\text{F}_1$ emission (S_6) at 582.4 nm (dashed line). All samples were annealed at 973 K during 3 h.

S_6 are superimposed. The presence of the $^7\text{F}_0 \rightarrow ^5\text{D}_{1a,b}$ (S_6) transitions in Figure 4A (ca. 523.5 and 526.0 nm, respectively) points to an efficient $\text{Eu}^{3+}(\text{S}_6)$ -to- $\text{Eu}^{3+}(\text{C}_2)$ energy transfer mechanism.

The total emission intensity originated from the excited $\text{Eu}^{3+}(\text{S}_6)$ ions, $I(\text{S}_6)$, is proportional to the amount of isolated and radiatively decaying $\text{Eu}^{3+}(\text{S}_6)$ centers and can be calculated from the spectrum recorded at 11 K and excited at 523.5 nm, i.e., $^7\text{F}_0 \rightarrow ^5\text{D}_{1b}$ (S_6) line. This intensity allows the estimation of the critical $\text{Eu}^{3+}(\text{S}_6) \rightarrow \text{Eu}^{3+}(\text{C}_2)$ energy-transfer distance, R_0 , assuming for any $\text{Eu}^{3+}(\text{S}_6) \rightarrow \text{Eu}^{3+}(\text{C}_2)$ pair, that the $\text{Eu}^{3+}(\text{S}_6)$ ions will decay radiatively if their separation is larger than R_0 and $\text{S}_6 \rightarrow \text{C}_2$ transfer will occur if it is smaller than R_0 . According to Buijs et al.^[43] if each $\text{Eu}^{3+}(\text{S}_6)$ has n neighboring Gd^{3+} sites within R_0 that can be occupied by a $\text{Eu}^{3+}(\text{C}_2)$, the probability for the $\text{Eu}^{3+}(\text{S}_6)$ ion to be isolated in Gd_2O_3 host is given by:

$$(100 - C)^n = \frac{I(\text{S}_6) \times 100}{I(\text{S}_6) + I(\text{C}_2)} \quad (1)$$

where C is the Eu^{3+} molar concentration. Given the n value and the structural Gd_2O_3 data,^[36] R_0 will be estimated. Figure 5A–C display the $I(\text{S}_6)$, n , and R_0 values for $\text{Gd}_2\text{O}_3:\text{Eu}^{3+}$ nanotubes (0.16%, 1.00%, 3.30%, and 6.60%), nanorods, and microcrystals. For similar Eu^{3+} content (3.30–3.65%), the intensity of the $\text{Eu}^{3+}(\text{S}_6)$ emission of the nanotubes is lower than the emissions of nanorods and microcrystals, suggesting that the number n of neighboring Gd^{3+} sites within R_0 that may be occupied by $\text{Eu}^{3+}(\text{C}_2)$ ions is larger for nanotubes with the consequent increase of the critical $\text{S}_6 \rightarrow \text{C}_2$ energy transfer distance R_0 (from 14.2 and 14.9 Å, in the microcrystals and nanorods, respectively, to 15.8 Å in the nanotubes). The intensity ratio of $\text{Eu}^{3+}(\text{S}_6)$ and $\text{Eu}^{3+}(\text{C}_2)$ emission lines decreases on increasing the Eu^{3+}

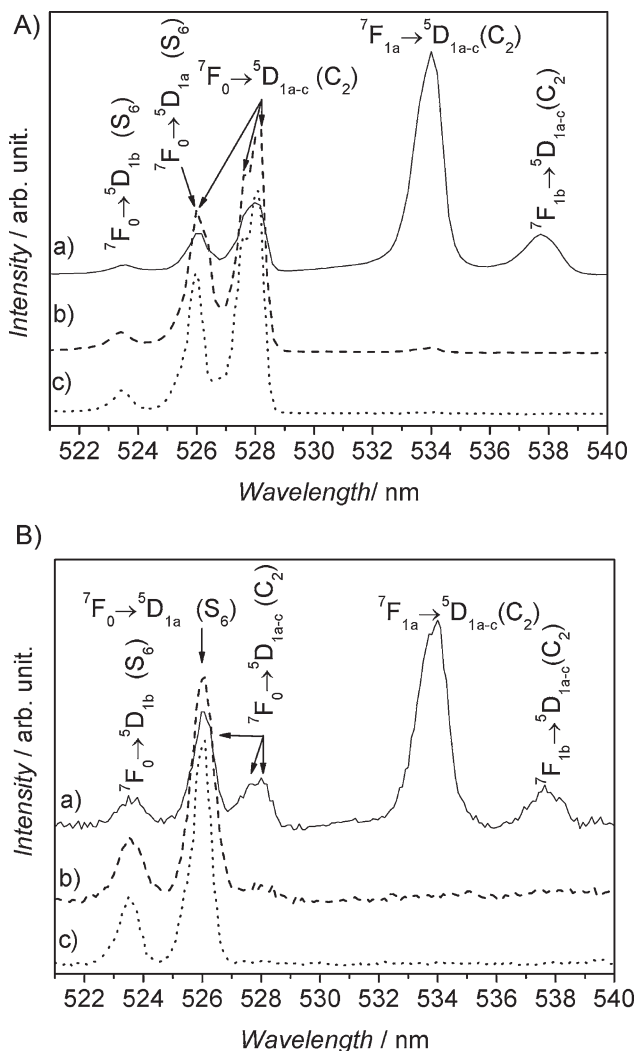


Figure 4. Excitation spectra (11 K) of $\text{Gd}_2\text{O}_3:\text{Eu}^{3+}$ expanded in the spectral region of the ${}^7\text{F}_{0,1} \rightarrow {}^5\text{D}_1$ transitions monitoring the A) ${}^5\text{D}_0 \rightarrow {}^7\text{F}_2$ emission (C_2) at 611.0 nm and B) ${}^5\text{D}_0 \rightarrow {}^7\text{F}_{1a}$ emission (S_6) at 582.4 nm from a) nanotubes (3.30%), b) nanorods (3.30%) and c) microcrystals (3.65%) in samples annealed at 973 K for 3 h. The spectral resolution is 1 nm; the slits used were 0.4 mm and the reciprocal linear density of the monochromator was 2.6 nm mm^{-1} .

Table 1. Room-temperature emission quantum yield of $\text{Gd}_2\text{O}_3:\text{Eu}^{3+}$ nanotubes (3.30%) and nanorods (3.30%), and microcrystals (3.65%) annealed at different conditions and measured upon wavelength excitation at 255 nm (LMCT band).

| Conditions | | Emission quantum yield | | |
|-----------------|----------|------------------------|----------|---------------|
| Temperature [K] | Time [h] | Nanotubes | Nanorods | Microcrystals |
| 923 | 3 | 0.51 | 0.44 | – |
| 923 | 6 | 0.51 | 0.46 | – |
| 973 | 3 | 0.51 | 0.50 | 0.70 |
| 973 | 6 | 0.54 | 0.56 | – |
| 1023 | 3 | 0.59 | 0.58 | – |
| 1023 | 6 | 0.54 | 0.53 | – |

content in the $\text{Gd}_2\text{O}_3:\text{Eu}^{3+}$ nanotubes (Fig. 5A). This observation, already reported for the bulk material by Buijs et al.,^[43] indicates an increasing rate of $\text{Eu}^{3+}(\text{S}_6) \rightarrow \text{Eu}^{3+}(\text{C}_2)$ energy transfer with the subsequent increase of the n neighboring Gd^{3+} sites within R_0 that may be occupied by $\text{Eu}^{3+}(\text{C}_2)$ ions (Fig. 5B) and of the critical $\text{S}_6 \rightarrow \text{C}_2$ energy transfer distance R_0 (Fig. 5C).

As far as we know, no data are available for $\text{Gd}_2\text{O}_3:\text{Eu}^{3+}$ nanocrystals, thus not allowing the comparison of $I(\text{S}_6)$, n , and R_0 values. However, for microcrystals, the $I(\text{S}_6)$ value measured in this work (9.5%) is smaller than that reported for analogous materials (11%),^[43] despite the smaller amount of incorporated Eu^{3+} (3.65% against 5%). Thus, in spite of the smaller number of active Eu^{3+} centers in the microcrystals synthesized in this work, the number n of neighboring Gd^{3+} sites within R_0 that may be occupied by $\text{Eu}^{3+}(\text{C}_2)$ ions and the R_0 values are larger than those previously reported,^[43] which suggests a clustering of Eu^{3+} ions at C_2 sites.

2.3. Anomalous Photoluminescence Features of $\text{Gd}_2\text{O}_3:\text{Eu}^{3+}$ and $\text{Gd}_2\text{O}_3:\text{Yb}^{3+}, \text{Er}^{3+}$ Nanotubes

In what follows, we discuss the intriguing and unprecedented anomalous thermalization of the ${}^7\text{F}_{1a,b}$ (Eu^{3+}) and ${}^2\text{H}_{11/2}$ (Er^{3+}) levels, in $\text{Gd}_2\text{O}_3:\text{Eu}^{3+}$ and $\text{Gd}_2\text{O}_3:\text{Yb}^{3+}, \text{Er}^{3+}$ nanotubes, respectively, which induces C_2 -to- S_6 energy transfer (Eu^{3+}) at 11 K and ${}^2\text{H}_{11/2} \rightarrow {}^4\text{I}_{15/2}$ upconversion emission (Er^{3+}), both of which were clearly unexpected. We stress that the photoluminescence measurements were all carried out within a week after preparing fresh samples. When the samples are kept in ambient atmosphere degradation of these anomalous properties started after ca. 7 days, and after ca. 70 days, no ${}^7\text{F}_{1a,b}$ population was observed at 11 K. Recalcination of the samples, using the synthesis conditions used for preparing the parent samples, recovers the anomalous behavior.

2.3.1. ${}^7\text{F}_{1a,b}$ and ${}^2\text{H}_{11/2}$ Population

An interesting aspect observed in the excitation spectra of $\text{Gd}_2\text{O}_3:\text{Eu}^{3+}$ nanotubes (3.30%, annealed at 973 K for 3 h) is the presence of the ${}^7\text{F}_{1a,b} \rightarrow {}^5\text{D}_1$ lines at temperatures below 80 K (Fig. 6A). For $\text{Gd}_2\text{O}_3:\text{Yb}^{3+}, \text{Er}^{3+}$ nanotubes (5.00% Yb^{3+} and 1.20% Er^{3+} , calcined at 973 K for 3 h), it is also remarkable to observe the ${}^2\text{H}_{11/2} \rightarrow {}^4\text{I}_{15/2}$ upconversion emission in the entire 11–300 K temperature range (Fig. 7A). The ratios of the ${}^7\text{F}_1/{}^7\text{F}_0$ (Eu^{3+}) and ${}^2\text{H}_{11/2}/{}^4\text{S}_{3/2}$ (Er^{3+}) populations (C_2 or S_6 sites) normally follow a Boltzmann distribution:

$$\frac{{}^7\text{F}_1 \rightarrow {}^5\text{D}_1}{{}^7\text{F}_0 \rightarrow {}^5\text{D}_1} \propto \exp(-\Delta E_1/kT) \quad \text{and} \quad \frac{{}^2\text{H}_{11/2} \rightarrow {}^4\text{I}_{15/2}}{{}^4\text{S}_{3/2} \rightarrow {}^4\text{I}_{15/2}} \propto \exp(-\Delta E_2/kT) \quad (2)$$

where k is the Boltzmann constant, T the temperature, and ΔE_1 and ΔE_2 the energy differences between the ${}^7\text{F}_0$ and the ${}^7\text{F}_1$ and the ${}^2\text{H}_{11/2}$ and ${}^4\text{S}_{3/2}$ levels (Scheme S1 and S2 (SI)), respectively. Thus, the ${}^7\text{F}_1$ and ${}^2\text{H}_{11/2}$ populations should be close to 0 at 11 K, as indeed observed by us for $\text{Gd}_2\text{O}_3:\text{Eu}^{3+}$ nanorods and microcrystals (Fig. 6B,C) and for $\text{Gd}_2\text{O}_3:\text{Yb}^{3+}, \text{Er}^{3+}$ nanotubes calcined at 923 K during 3 h (Fig. 7B) and by Liu et al. for analogous $\text{Gd}_2\text{O}_3:\text{Eu}^{3+}$ nanorods (5% Eu^{3+} , annealed at 973 K for

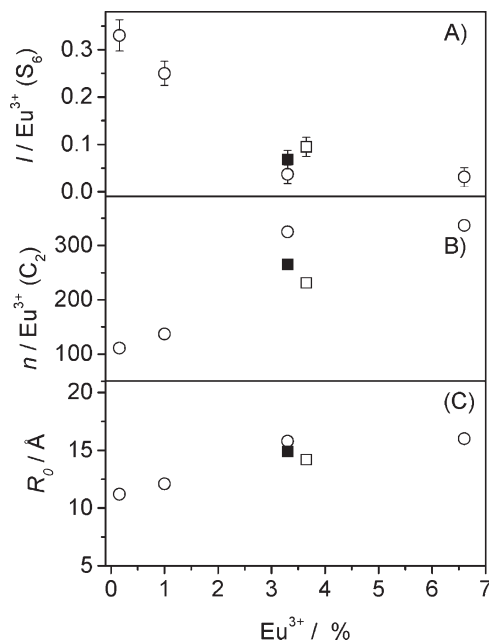


Figure 5. Influence of Eu^{3+} content on A) $I(S_6)$, B) number n of Gd^{3+} neighbors occupied by Eu^{3+} (C_2) ions, and C) R_0 for $\text{Gd}_2\text{O}_3:\text{Eu}^{3+}$ nanotubes (○: 0.16% and 1.00% annealed at 923 K for 6 h, 3.30% at 973 K for 3 h, and 6.60% at 1123 K for 6 h), nanorods (■: 3.30%, 973 K for 3 h) and microcrystals (□: 3.65%, 973 K for 3 h).

1 h).^[19] However, the ${}^7\text{F}_1 \rightarrow {}^5\text{D}_1$ lines dominate the 11 K excitation spectra of Figure 6A, and the ${}^2\text{H}_{11/2} \rightarrow {}^4\text{I}_{15/2}$ upconversion emission in Figure 7A displays intensity similar to that of the ${}^4\text{S}_{3/2} \rightarrow {}^4\text{I}_{15/2}$ lines. Although this anomalous thermalization effect has been previously reported for $\text{Gd}_2\text{O}_3:\text{Eu}^{3+}$ nanotubes^[14] and $\text{Y}_2\text{O}_3:\text{Er}^{3+}$ nanocrystals,^[27,28] it is one order of magnitude stronger for our best $\text{Gd}_2\text{O}_3:\text{Eu}^{3+}$ nanotubes (0.16% Eu^{3+} annealed at 923 K for 6 h, 3.30% at 973 K for 3 h and 6.60% at 1123 K for 6 h, see below). Moreover, as far as we know, there are no previous reports illustrating anomalous thermalization effects in high-energy ${}^7\text{F}_1$ Stark components (352 cm^{-1} above ${}^7\text{F}_0$) and in the ${}^2\text{H}_{11/2}$ Er^{3+} excited level (Fig. 6A and 7A).

To ensure that the spectra of nanotubes, nanorods, and microcrystals were measured in identical experimental conditions and at the same temperature of 11 K the following procedure was adopted:

- Thin (<0.5 mm), identically sized, pellets of $\text{Gd}_2\text{O}_3:\text{Eu}^{3+}$ nanotubes and microcrystals (or nanorods) (3.30% of Eu^{3+} content annealed at 973 K for 3 h) were placed 0.3 mm apart in the same cryostat holder and cooled to 11 K.
- Excitation spectra of both pellets were recorded, monitoring the ${}^5\text{D}_0 \rightarrow {}^7\text{F}_2(C_2)$ line at 611.0 nm, by moving the cryostat horizontally. In this way, the ${}^7\text{F}_{1a,b} \rightarrow {}^5\text{D}_1(C_2)$ transition lines were detected for the nanotubes and not detected for microcrystals and nanorods (Scheme S3 (SI)), excluding, therefore, the possibility that the samples are at an elevated temperature in the cryostat. The latter is also supported by the fact that the intensity ratio of hot-to-normal bands remains unchanged when the incident power of the Xe lamp is attenuated by inserting neutral density filters.

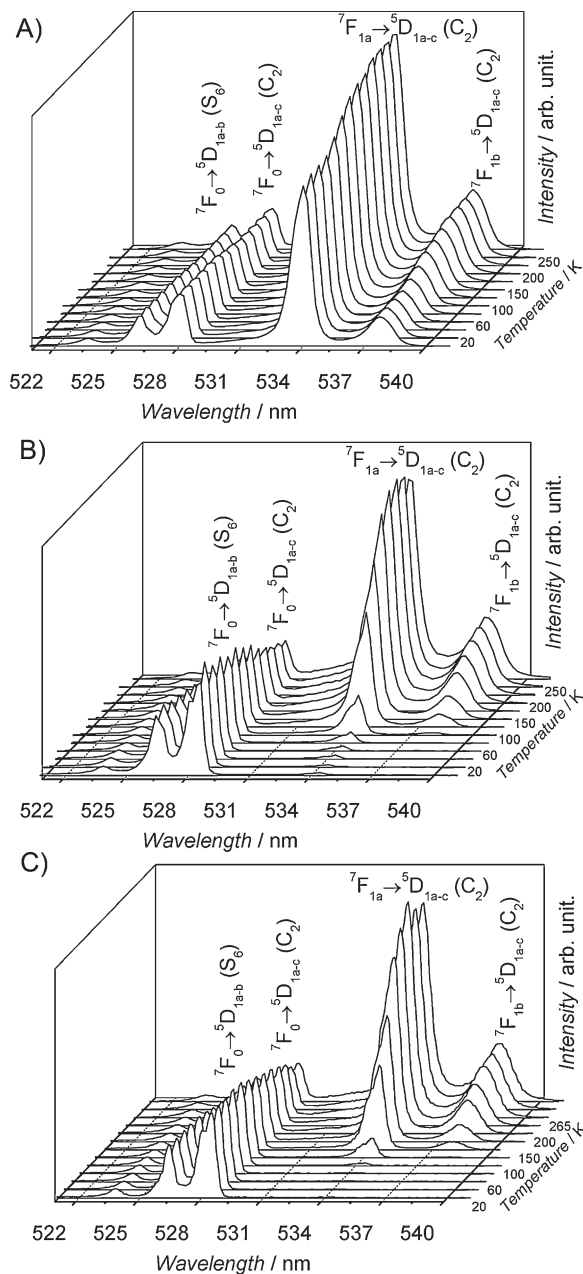


Figure 6. Expanded ${}^7\text{F}_{0,1} \rightarrow {}^5\text{D}_1$ excitation spectra acquired monitoring the ${}^5\text{D}_0 \rightarrow {}^7\text{F}_2(C_2)$ emission at 611 nm from A) nanotubes (3.30%), B) nanorods (3.30%) and C) microcrystals (3.65%) as function of temperature; samples annealed at 973 K for 3 h.

The temperature dependence of the integrated intensity ratio of hot-to-normal bands as a function of the annealing conditions is shown in Figure 8 and 9 for the $\text{Gd}_2\text{O}_3:\text{Eu}^{3+}$ (3.30% Eu^{3+}) and $\text{Gd}_2\text{O}_3:\text{Yb}^{3+},\text{Er}^{3+}$ nanotubes (5.00% Yb^{3+} and 1.20% Er^{3+}), respectively. The integrated intensities are calculated fitting the Eu^{3+} ${}^7\text{F}_0 \rightarrow {}^5\text{D}_1(S_6)$ and ${}^7\text{F}_{0,1a,b} \rightarrow {}^5\text{D}_1(C_2)$ transitions (acquired monitoring the ${}^5\text{D}_0 \rightarrow {}^7\text{F}_2(C_2)$ emission at 611.0 nm) and the Er^{3+} upconversion ${}^2\text{H}_{11/2} \rightarrow {}^4\text{I}_{15/2}$ and ${}^4\text{S}_{3/2} \rightarrow {}^4\text{I}_{15/2}$ lines using Gaussian functions. The temperature dependence of the

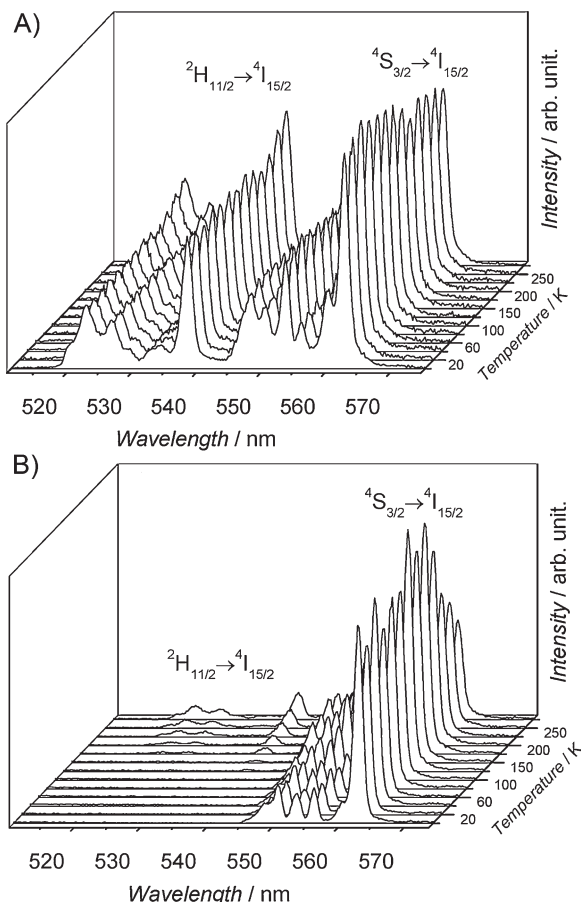


Figure 7. Expanded upconversion emission spectra upon laser excitation (980 nm) in the $^4S_{3/2}$, $^2H_{11/2} \rightarrow ^4I_{15/2}$ region of $Gd_2O_3:Yb^{3+},Er^{3+}$ (5.00% Yb^{3+} and 1.20% Er^{3+}) nanotubes calcined at A) 973 and B) 923 K for 3 h.

$^2H_{11/2} \rightarrow ^4I_{15/2}/^4S_{3/2} \rightarrow ^4I_{15/2}$ integrated intensity ratio of the nanocrystals calcined at 973 K for 3 h is rather anomalous and constant between 11 and 250 K. In contrast, the temperature dependence of this ratio for the nanotubes calcined at 923 K displays the expected Boltzmann distribution with $\Delta E_2(^2H_{11/2} \rightarrow ^4S_{3/2}) = 700 \text{ cm}^{-1}$. The intensity ratio between the $^2H_{11/2} \rightarrow ^4I_{15/2}$ and $^4S_{3/2} \rightarrow ^4I_{15/2}$ transitions remains essentially unchanged as the power of the diode laser increases from 0.4 to 1 W indicating negligible thermal effects arising from the excitation laser.

The temperature dependence of the $^7F_{1a} \rightarrow ^5D_1/7F_0 \rightarrow ^5D_1$ ($^7F_{1a}$ at 217 cm^{-1} above 7F_0) integrated intensity ratio (R_a) of the samples calcined at 923 K for 3 and 6 h, and at 1023 K for 6 h, is similar to that previously quoted by Liu et al.,^[14] i.e., an intensity ratio of ca. 0.03 at 11 K. However, the sample calcined at 973 K for 3 h exhibits abnormal temperature dependence for the R_a ratio, being almost constant below 115 K and one order of magnitude larger (~ 0.49) than that observed for the other samples (Fig. 8).

For each Eu^{3+} nanotube content, the maximum value of the 11 K R_a ratio depends on the annealing conditions (time and temperature) and it may even be zero. The temperature dependence of these maxima is shown for three Eu^{3+} contents

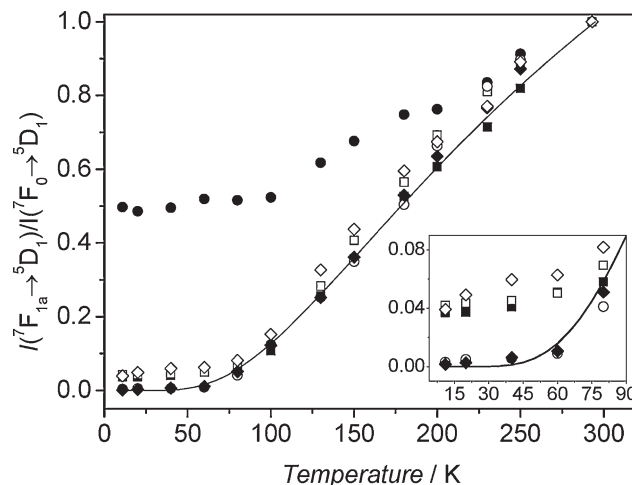


Figure 8. Normalized relative intensity ratio between the $^7F_{1a} \rightarrow ^5D_1$ and $^7F_0 \rightarrow ^5D_1$ transitions of $Gd_2O_3:Eu^{3+}$ nanotubes (3.30%), monitored at 611 nm ($^5D_0 \rightarrow ^7F_2$ line of the Eu^{3+} ions in the C_2 local symmetry), versus temperature. Annealing parameters: 923 K for 3 h (■); 923 K for 6 h (□); 973 K for 3 h (●); 973 K for 6 h (○); 1023 K for 3 h (◆); 1023 K for 6 h (◇). The inset shows a magnification of the low-temperature region for all the samples with the exception of that calcined at 973 K for 3 h. The full lines are Boltzmann distributions (Eq. 2) considering $\Delta E = 217 \text{ cm}^{-1}$.

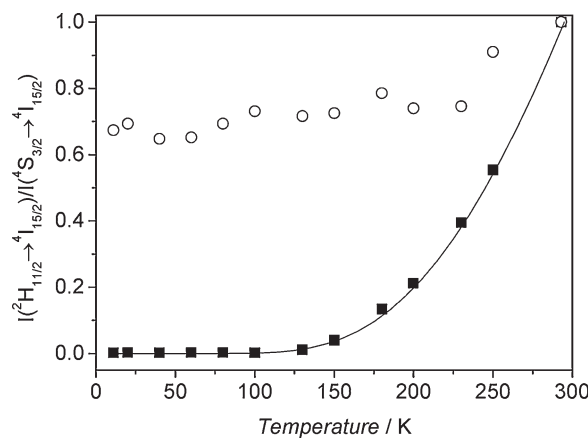


Figure 9. Normalized relative intensity ratio between the $^2H_{11/2} \rightarrow ^4I_{15/2}$ and $^4S_{3/2} \rightarrow ^4I_{15/2}$ transitions of $Gd_2O_3:Yb^{3+},Er^{3+}$ nanotubes (5.00% Yb^{3+} and 1.20% Er^{3+}), excited at 980 nm via Yb^{3+} -to- Er^{3+} energy transfer, versus temperature. Annealing parameters: 923 K for 3 h (■); 973 K for 3 h (○). The full line is a Boltzmann distribution (Eq. 2) considering $\Delta E = 700 \text{ cm}^{-1}$.

in Figure 10A. Figure 10B exhibits the temperature dependence of the $^7F_{1b} \rightarrow ^5D_1/7F_0 \rightarrow ^5D_1$ intensity ratios (R_b) for the same set of samples shown in Figure 10A. It is quite remarkable that the $^7F_{1b}$ level (at 352 cm^{-1} above 7F_0) is still populated at low temperatures, also displaying an anomalous thermalization effect. However, the R_b ratio at 11 K is lower than the corresponding R_a (e.g., 0.32 for the sample calcined at 973 K for 3 h, Fig. 10B). The temperature range where it is almost constant is also slightly lower ($\sim 90 \text{ K}$). For

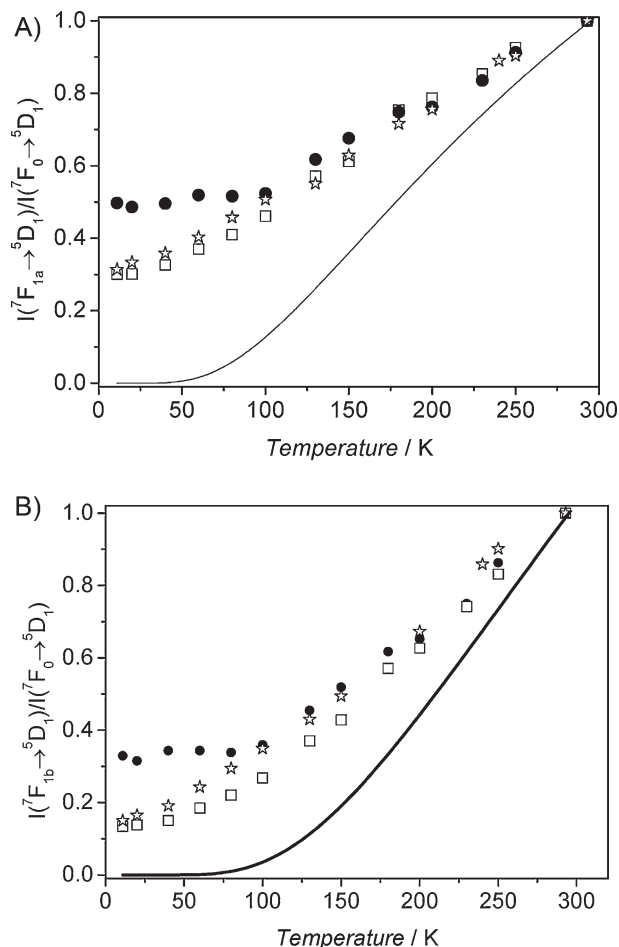


Figure 10. Influence of Eu^{3+} content on the maximum values of normalized relative intensity ratio of the A) ${}^7\text{F}_{1a} \rightarrow {}^5\text{D}_1$ and ${}^7\text{F}_0 \rightarrow {}^5\text{D}_1$ lines or B) ${}^7\text{F}_{1b} \rightarrow {}^5\text{D}_1$ and ${}^7\text{F}_0 \rightarrow {}^5\text{D}_1$ lines in $\text{Gd}_2\text{O}_3:\text{Eu}^{3+}$ nanotubes. (\square): 0.16% annealed at 923 K for 6 h; (\bullet): 3.30% at 973 K for 3 h, and (\star): 6.60% at 1123 K for 6 h). The full lines are Boltzmann distributions (Eq. 2) considering $\Delta E = 217 \text{ cm}^{-1}$ and ${}^7\text{F}_{1a} \rightarrow {}^7\text{F}_0(\text{C}_2)$ (A) or $\Delta E = 352 \text{ cm}^{-1}$ and ${}^7\text{F}_{1b} \rightarrow {}^7\text{F}_0(\text{C}_2)$ (B).

all the other samples studied, the ${}^7\text{F}_{1b}$ population is thermalized and R_b follows the expected Boltzmann trend.

2.3.2. $\text{Eu}^{3+}(\text{C}_2)$ to $\text{Eu}^{3+}(\text{S}_6)$ Energy Transfer at 11 K

In contrast with a previous report,^[14] for Eu^{3+} contents above 3.30% and samples annealed at 973 K for 3 h, back transfer from $\text{Eu}^{3+}(\text{C}_2)$ to $\text{Eu}^{3+}(\text{S}_6)$ occurs efficiently in the $\text{Gd}_2\text{O}_3:\text{Eu}^{3+}$ nanotubes at 11 K, as shown by the three groups of $\text{Eu}^{3+}(\text{C}_2)$ transitions observed at ca. 527–528 nm (${}^7\text{F}_0 \rightarrow {}^5\text{D}_1$), 533–535 nm (${}^7\text{F}_{1a} \rightarrow {}^5\text{D}_1$), and 537–539 nm (${}^7\text{F}_{1b} \rightarrow {}^5\text{D}_1$) in the site-selective excitation spectra of Figure 4B and 11, monitoring the $\text{D}_0 \rightarrow {}^7\text{F}_1(\text{S}_6)$ emission at 582.4 nm. We note that nanorods also exhibit the $\text{Eu}^{3+}(\text{C}_2)$ -to- $\text{Eu}^{3+}(\text{S}_6)$ energy transfer, although much weaker (faint ${}^7\text{F}_0 \rightarrow {}^5\text{D}_1$ line, Fig. 4B). Because the energy difference between the ${}^5\text{D}_0$ levels of Eu^{3+} in both sites (ca. 100 cm^{-1} for microcrystals^[43]) cannot be bridged thermally at 11 K, some other mechanism must be operative. As both ${}^7\text{F}_{1a,b}(\text{C}_2)$ levels are populated at low temperatures, transitions to the ${}^5\text{D}_1(\text{C}_2)$ levels

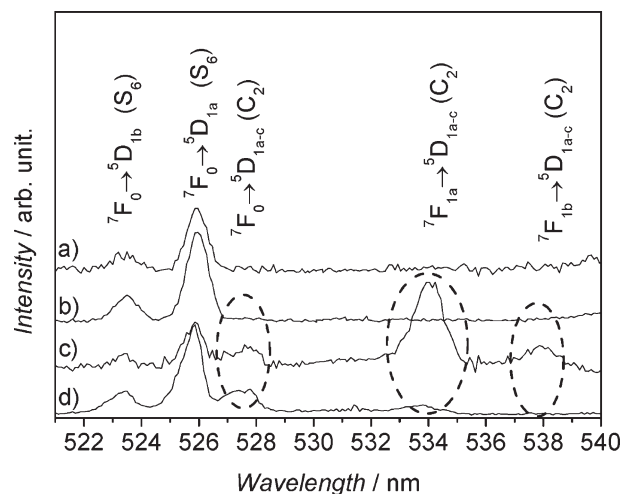


Figure 11. Expanded 11 K excitation spectra recorded while monitoring the ${}^5\text{D}_0 \rightarrow {}^7\text{F}_{1a}$ emission (S_6) at 582.4 nm of $\text{Gd}_2\text{O}_3:\text{Eu}^{3+}$ nanotubes containing a) 0.16%, b) 1.00%, c) 3.30%, and d) 6.60% Eu^{3+} ; samples annealed at 973 K for 3 h.

become possible, allowing then subsequent energy transfer to the resonant ${}^5\text{D}_{1a}(\text{S}_6)$ excited state (Scheme S1 (SI)).

2.4. Rationalizing the Anomalous Photoluminescence Features

We now attempt to rationalize the anomalous thermalization effect on the basis of phonon confinement in nanocrystals.^[14,26–29] We start by stressing that TEM and XRD did not indicate any significant differences in the morphology (diameter, wall thickness, and nanocrystallite size) and crystal structure of samples exhibiting or not exhibiting anomalous thermalization. The PDOS in nanocrystals is discrete and the low-frequency acoustical phonons cut-off (ν_{\min}) depends on the particles radius R as:^[29]

$$\nu_{\min} = 2.05 \frac{\nu_s}{2\pi R} \quad (3)$$

where ν_s is the sound velocity (5000 ms^{-1} in Gd_2O_3). Equation 3 is related to the classical approach of Lamb in which an isolated spherical nanoparticle of diameter d cannot support internal vibrations at frequencies less than the so-called Lamb mode frequency, $\nu_L = \frac{2\pi\nu_s}{d}$.^[27] Considering a 1D phonon confinement perpendicular to the nanotubes wall with a thickness of ca. 5 nm the phonon cut-off frequency is estimated based on Equation 3 to be ca. 23 cm^{-1} .^[14] Thus, it is expected that the PDOS should also be discrete and ca. 220 cm^{-1} and as a result, the ${}^7\text{F}_{1a}$ and ${}^7\text{F}_{1b}$ levels of the $\text{Gd}_2\text{O}_3:\text{Eu}^{3+}$ nanotubes are not depopulated; the direct phonon relaxation is restricted (much less in the ${}^7\text{F}_{1b}$ level at $\sim 350 \text{ cm}^{-1}$). This explanation seems adequate to rationalize the anomalous thermalization effect measured by us in the samples with lower R_a (3.30%, calcined at 923 K for 3 and 6 h, and at 1023 K for 6 h) and also by Liu et al. in analogous $\text{Gd}_2\text{O}_3:\text{Eu}^{3+}$ nanotubes (3.96%, annealing at 773 K for 1 h).^[14] However, in the

$\text{Gd}_2\text{O}_3:\text{Eu}^{3+}$ nanotubes with 0.16% annealed at 923 K for 6 h, 3.30% 973 K for 3 h, and 6.60% 1123 K for 6 h, the effect we observe is ca. 10–16 times larger, and thus, the phonon cut-off frequency resulting from the (above-mentioned) 1D phonon confinement *perpendicular* to the nanotubes wall does not fully account for it. Moreover, the anomalous thermalization of the $^2\text{H}_{11/2}$ level in the $\text{Gd}_2\text{O}_3:\text{Yb}^{3+},\text{Er}^{3+}$ nanotubes also could not be rationalized based only on the 1D phonon confinement *perpendicular* to the nanotubes wall that restricts the direct phonon relaxation from the $^2\text{H}_{11/2}$ level to the $^4\text{S}_{3/2}$ one, involving a three-phonon process with a single-phonon energy around 230–240 cm^{-1} ^[28] (intriguingly a value similar to the $^7\text{F}_0$ – $^7\text{F}_1$ energy difference previously discussed).

As a further effect from these confinements, the discrete features of the PDOS (approximately modeled by a sequence of discrete sharp peaks^[27–29]) may play a crucial role in the $^7\text{F}_{1a,1b}$ and $^2\text{H}_{11/2}$ thermal populations. The energy matching between the available phonons frequency and the Eu^{3+} and Er^{3+} electronic levels provides a route to their thermalization (depopulating process). Slight changes in the structure of the nanotubes (for instance, due to thermal treatment or modifications in the Eu^{3+} or $\text{Yb}^{3+}/\text{Er}^{3+}$ content) may induce considerable changes in the discrete PDOS, thus completely modifying the energy resonance conditions and the intensity ratio values. For sizes of ca. 5 nm, for instance, abrupt changes of more than one order of magnitude from PDOS maxima to almost zero values with small changes of phonon energy are profuse in the PDOS discrete spectra of Y_2O_3 nanocrystals (see Fig. 2 of Ref. [29]).

Moreover, the different values obtained for the R_a and R_b ratios of $\text{Gd}_2\text{O}_3:\text{Eu}^{3+}$ nanotubes may also be explained by this extra resonant effect, indicating that the two $^7\text{F}_{1a,1b}$ electronic levels have distinct anomalous thermalizations. For R_b , the effect of PDOS discretization is less effective because the PDOS spectra exhibit a baseline at higher energies. In principle, the exposure of the nanotubes to the ambient moisture would produce an amorphous layer at the surface of the nanotubes, increasing the effective wall thickness and broadening the PDOS spectra. Eventually, this would destroy the nanoconfinement conditions, and therefore, the thermalization behavior of the $^7\text{F}_1$ level will be similar to that of the $\text{Gd}_2\text{O}_3:\text{Eu}^{3+}$ nanorods.

A quantitative analysis of this effect (beyond the scope of the present paper) should take into account the presence of nanometer-sized clusters (smaller than 5 nm) in the walls of the Gd_2O_3 nanotubes, which may reduce the cut-off frequency of the phonons.

Although Ln^{3+} -rich nanometer-sized clusters may, in principle, also form in $\text{Gd}_2\text{O}_3:\text{Eu}^{3+}$ and $\text{Gd}_2\text{O}_3:\text{Yb}^{3+},\text{Er}^{3+}$ nanorods and microcrystals, the anomalous thermalization effect is absent because the clusters are embedded in extended 3D Gd_2O_3 domains, where no specific direction for 1D phonon confinement may be defined, with the ensuing modifications in the phonon density of states (the 3D Gd_2O_3 regions behave as a thermal bath depopulating the $^7\text{F}_1$ and $^2\text{H}_{11/2}$ levels).

3. Conclusions

$\text{Gd}_2\text{O}_3:\text{Eu}^{3+}$ (0.16%, 1.00%, 3.30%, and 6.60% Eu^{3+} molar content) and $\text{Gd}_2\text{O}_3:\text{Yb}^{3+},\text{Er}^{3+}$ (5.00% Yb^{3+} , 1.20% Er^{3+})

nanotubes, $\text{Gd}_2\text{O}_3:\text{Eu}^{3+}$ nanorods (3.30%) and $\text{Gd}_2\text{O}_3:\text{Eu}^{3+}$ microcrystals (3.65%) have been obtained by hydrothermal synthesis using different annealing conditions, 923–1123 K, and time interval ranging from 3 to 6 h. For nanotubes, the role of the ion–phonon interaction on the photoluminescence features and excited-state dynamics is completely different from the role for nanorods and microcrystals, due to the absence of low-frequency phonon modes. Hot bands arising from the two lowest-lying $^7\text{F}_1$ Eu^{3+} crystal-field levels are observed in the excitation spectra of $\text{Gd}_2\text{O}_3:\text{Eu}^{3+}$ nanotubes with intensity higher than the corresponding bands originated in the $^7\text{F}_0$ ground state between 300 and 11 K. For $\text{Gd}_2\text{O}_3:\text{Yb}^{3+},\text{Er}^{3+}$ nanotubes, hot bands arising from the $^2\text{H}_{11/2}$ Er^{3+} level are also present in the emission spectra measured in that same temperature range with intensities similar to the ones originated in the $^4\text{S}_{3/2}$ low-energy level. These remarkable anomalous thermalization effects, which are strongly dependent on the thermal history of the samples and on the Eu^{3+} or $\text{Yb}^{3+}/\text{Er}^{3+}$ contents, are one order of magnitude larger than previously reported for similar $\text{Gd}_2\text{O}_3:\text{Eu}^{3+}$ (3.96%, annealing at 773 K, 1 h) nanotubes.

The anomalous thermalization may be rationalized on the basis of the theoretical framework of ion–lattice interaction considering both, the 1D phonon confinement *perpendicular* to the nanotubes wall (as previously proposed for $\text{Gd}_2\text{O}_3:\text{Eu}^{3+}$ nanotubes), and the discrete features of the phonon density of states. The energy matching between the frequency of the available phonons and the $^7\text{F}_{1a,1b}$ and $^2\text{H}_{11/2}$ electronic levels provides a route to their thermalization (depopulating process). Minor changes in the structure of the nanotubes (due to thermal treatment or Ln^{3+} content), which are hard to observe by XRD and TEM, may induce considerable changes in the discrete phonon density of states, entirely modifying the energy resonance conditions and the intensity ratio values between normal and hot bands.

The confinement of the electron–phonon interaction in nanocrystals impacts other aspects of the luminescence dynamics of lanthanide ions that depend on the low-energy phonon modes of the lattice (e.g., in phonon-assisted energy transfer and upconversion processes). Therefore, a fundamental understanding of the effects of phonon confinement on the luminescence features is crucial, particularly in systems, such as $\text{Gd}_2\text{O}_3:\text{Eu}^{3+}$ and $\text{Gd}_2\text{O}_3:\text{Yb}^{3+},\text{Er}^{3+}$ nanotubes, which have been used as fluorescent markers in a variety of immunosensing applications.

4. Experimental

Synthesis: $\text{Gd}_2\text{O}_3:\text{Eu}^{3+}$ nanocrystals (tubes and rods) and microcrystals were obtained through hydrothermal synthesis. In a typical synthesis, an aqueous solution containing $\text{Eu}(\text{NO}_3)_3 \cdot 5\text{H}_2\text{O}$ (0.19 mmol) and $\text{Gd}(\text{NO}_3)_3 \cdot 6\text{H}_2\text{O}$ (4.2 mmol) was prepared, in order to obtain an Eu^{3+} molar concentration of 3.30% (nanocrystals) and 3.65% (microcrystals). Then a NaOH solution (1 M) was added (final pH adjusted to 12.5–13), and the mixture was stirred for 1 h. The resultant white gel was transferred to a Teflon autoclave (inner volume 42 mL) and placed in a furnace at 393 K for 15 h (nanotubes), 423 K for 48 h (nanorods), and 503 K for 48 h (microcrystals). White precipitates were then filtered, washed with distilled water, and dried in air at 333 K. Dried powder (from nanocrystals: ~1.8 g) was divided in six portions (ca. 0.3 g), each of which was annealed independently in air at 923, 973 or 1023 K for 3 or 6 h, in a muffle furnace preheated at 313 K and with a heating rate of 5 K min^{-1} . Nanotubes with a Eu^{3+} molar content of 0.16%, 1.00%, and 6.60% were also prepared and

thermally treated in the above-mentioned conditions described. Furthermore the nanotubes with 6.60% of Eu^{3+} molar content received an addition annealing at 1123 K for 6 h. A similar procedure was adopted for the synthesis of $\text{Gd}_2\text{O}_3\cdot\text{Yb}^{3+},\text{Er}^{3+}$ nanotubes. In this case, solutions with $\text{Gd}(\text{NO}_3)_3\cdot 6\text{H}_2\text{O}$ (4.2 mmol), $\text{Yb}(\text{NO}_3)_3\cdot 5\text{H}_2\text{O}$ (0.26 mmol), and $\text{Er}(\text{NO}_3)_3\cdot 5\text{H}_2\text{O}$ (0.055 mmol) were prepared to obtain nanotubes with Yb 5.00% and Er 1.20% molar concentration. Then a NaOH solution (1 M) was added (final pH adjusted to 13) and the mixture was stirred for 1 h. The resultant white gel was transferred to a Teflon autoclave (inner volume 42 mL) and placed in a furnace at 393 K for 15 h. The white precipitates were then filtered, washed with distilled water, and dried in air at 333 K. Two portions of this dried powder (~ 0.3 g) were annealed independently in air at 923 or 973 K for 3 h, in a muffle furnace pre-heated at 313 K and with a heating rate of 5 K min^{-1} .

Powder X-ray Diffraction: XRD patterns were recorded using a Philips X'Pert MPD powder X-ray diffractometer. The samples were exposed to the $\text{Cu K}\alpha$ radiation (1.54 \AA) in a 2θ range of $1\text{--}60^\circ$ with a step of 0.04° and resolution of 40 s per step. Lanthanum hexaboride was used as a standard for d-spacing calibration.

Transmission Electron Microscopy: The morphology was analyzed on a Hitachi H9000-NA TEM microscope, and electron diffraction measurements were done on amorphous carbon-Fomvar grid support. The HRTEM image was recorded at the Department of Inorganic Chemistry, Fritz-Haber-Institute of the Max-Planck-Society in Berlin, on a Philips CM 200 (200 kV, $\text{Cs} = 1.35\text{ mm}$), equipped with a field-emission gun and a GATAN Tridiem image filter. The samples were previously dispersed in distilled water with ultrasonic stirring for 10 min. The TEM grid was deep-coated in this suspension and dried in air. The samples are sensitive to the electron beam and some signs of degradation were discerned after ~ 5 min.

Thermogravimetry Analysis (TGA): TGA were carried out using a Shimadzu TGA 50 instrument with a heating rate of 10 K min^{-1} under a continuous air stream with a flow rate of $10\text{ cm}^3\text{ min}^{-1}$.

Elemental Analysis: The Eu, Er, and Yb content were obtained using inductively coupled plasma optical emission spectroscopy (ICP-OES) on a Horiba Jobin-Yvon Activa-M instrument.

Photoluminescence: Emission and excitation spectra were recorded between 11 K and room-temperature on a Fluorolog-3 Jobin Yvon-Spex (Model FL3-2T) with a modular double grating excitation spectrometer (fitted with a $1200\text{ grooves mm}^{-1}$ grating blazed at 330 nm) and a TRIAX 320 single-emission monochromator (fitted with a $1200\text{ grooves mm}^{-1}$ grating blazed at 500 nm, reciprocal linear density of 2.6 nm mm^{-1}), coupled to a R928 Hamamatsu photomultiplier, using the front face acquisition mode. The excitation source was a 450 W Xe arc lamp, except for the upconversion emission in which a 980 nm diode laser was used. The emission spectra were corrected for detection and optical spectral response of the spectrofluorimeter, and the excitation spectra were corrected for the spectral distribution of the lamp intensity using a photodiode reference detector. Time-resolved measurements were carried out with the setup described for the luminescence spectra using a pulsed Xe-Hg lamp (6 μs pulse at half width and 20–30 μs tail). The measurements were performed using a He closed cycle cryostat and the temperature was increased in steps of 10 K using a Lakeshore 330 auto tuning temperature controller with a resistance heater. All samples were measured within ~ 7 days after synthesis.

Absolute Emission Quantum Yields: The quantum yields were measured at room-temperature using a quantum yield measurement system C9920-02 from Hamamatsu with a 150 W Xenon lamp coupled to a monochromator for wavelength discrimination, an integrating sphere as sample chamber and a multichannel analyzer for signal detection. Three measurements were made for each sample so that the average value is reported. The method is accurate within 10%.

Acknowledgements

We acknowledge the financial support of PTDC, FEDER, FSE and FCT (SFRH/BD/28433/2006) and P. Rawel and M. Willinger for help with TEM.

Supporting Information is available online from Wiley InterScience or from the authors.

Received: September 18, 2009
Published online: January 21, 2010

- [1] K. Binnemans, C. Gorller-Walrand, *Chem. Rev.* **2002**, 102, 2303.
- [2] C. Feldmann, T. Justel, C. R. Ronda, P. J. Schmidt, *Adv. Funct. Mater.* **2003**, 13, 511.
- [3] J.-C. G. Bünzli, C. Piguet, *Chem. Soc. Rev.* **2005**, 34, 1048.
- [4] L. D. Carlos, R. A. S. Ferreira, V. de Zea Bermudez, S. J. L. Ribeiro, *Adv. Mater.* **2009**, 21, 509.
- [5] F. Wang, X. Liu, *Chem. Soc. Rev.* **2009**, 38, 976.
- [6] Y. P. Fang, A. W. Xu, L. P. You, R. Q. Song, J. C. Yu, H. X. Zhang, Q. Li, H. Q. Liu, *Adv. Funct. Mater.* **2003**, 13, 955.
- [7] Q. Tang, J. Shen, W. Zhou, W. Zhang, W. Yu, Y. Qian, *J. Mater. Chem.* **2003**, 13, 3103.
- [8] M. Yada, M. Mihara, S. Mouri, M. Kuroki, T. Kijima, *Adv. Mater.* **2002**, 14, 309.
- [9] M. Yada, C. Taniguchi, T. Torikai, T. Watari, S. Furuta, H. Katsuki, *Adv. Mater.* **2004**, 16, 1448.
- [10] X. Bai, H. Song, L. Yu, L. Yang, Z. Liu, G. Pan, S. Lu, X. Ren, Y. Lei, L. Fan, *J. Phys. Chem. B* **2005**, 109, 15236.
- [11] X. Bai, H. Song, G. Pan, Z. Liu, S. Lu, W. Di, X. Ren, Y. Lei, Q. Dai, L. Fan, *Appl. Phys. Lett.* **2006**, 88, 143104.
- [12] X. Wang, J. Zhuang, Y. Li, *Eur. J. Inorg. Chem.* **2004**, 946.
- [13] Q. Kuang, Z. W. Lin, W. Lian, Z. Y. Jiang, Z. X. Xie, R. B. Huang, L. S. Zheng, *J. Solid State Chem.* **2007**, 180, 1236.
- [14] L. Liu, E. Ma, R. Li, G. Liu, X. Chen, *Nanotech.* **2007**, 18, 015403.
- [15] X. Bai, H. Song, G. Pan, X. Ren, B. Dong, Q. Dai, L. Fan, *J. Nanosci. Nanotechnol.* **2009**, 9, 2677.
- [16] H. Guo, N. Dong, M. Yin, W. Zhang, L. Lou, S. Xia, *J. Phys. Chem. B* **2004**, 108, 19205.
- [17] G. Liu, X. Chen, in: *Spectroscopic Properties of Lanthanides in Nanomaterials*, Handbook on the Physics and Chemistry of Rare Earths, Vol. 37 (Eds: K. A. Gschneidner Jr, J.-C. G. Bünzli, V. K. Pecharsky), Elsevier B.V, Amsterdam, The Netherlands **2007**, p. 99.
- [18] L. Liu, X. Chen, *Nanotech.* **2007**, 18, 255704.
- [19] L. Liu, E. Ma, R. Li, X. Chen, *J. Nanosci. Nanotechnol.* **2008**, 8, 1398.
- [20] X. Chen, E. Ma, G. Liu, M. Yin, *J. Phys. Chem. C* **2007**, 111, 9638.
- [21] X. Chen, E. Ma, G. Liu, *J. Phys. Chem. C* **2007**, 111, 10404.
- [22] C. Liu, J. Liu, K. Dou, *J. Phys. Chem. B* **2006**, 110, 20277.
- [23] B. M. Tissue, *Chem. Mater.* **1998**, 10, 2837.
- [24] B. Mercier, C. Dujardin, G. Ledoux, C. Louis, O. Tillement, *J. Appl. Phys.* **2004**, 96, 650.
- [25] B. Mercier, G. Ledoux, C. Dujardin, D. Nicolas, B. Masenelli, P. Mélinon, G. Bergeret, *J. Chem. Phys.* **2007**, 126, 044507.
- [26] B. Mercier, C. Dujardin, G. Ledoux, C. Louis, O. Tillement, P. Perriat, *J. Lumin.* **2006**, 119–120, 224.
- [27] G. K. Liu, H. Z. Zhuang, X. Y. Chen, *Nano Lett.* **2002**, 2, 535.
- [28] G. K. Liu, X. Y. Chen, H. Z. Zhuang, S. Li, R. S. Niedbala, *J. Solid State Chem.* **2003**, 171, 123.
- [29] X. Y. Chen, Z. Zhuang, G. K. Liu, S. Li, R. S. Niedbala, *J. Appl. Phys.* **2003**, 94, 5559.
- [30] R. S. Meltzer, K. S. Hong, *Phys. Rev. B* **2000**, 61, 3396.
- [31] E. Downing, L. Hesselink, J. Ralston, R. Macfarlane, *Science* **1996**, 273, 1185.
- [32] L. Wang, Y. Li, *Nano Lett.* **2006**, 6, 1645.
- [33] A. Bettencourt-Dias, *Dalton Trans.* **2007**, 2229.
- [34] K. T. Yong, I. Roy, M. T. Swihart, P. N. Prasad, *J. Mater. Chem.* **2009**, 19, 4655.
- [35] Z. Chen, H. Chen, H. Hu, M. Yu, F. Li, Q. Zhang, Z. Zhou, T. Yi, C. Huang, *J. Am. Chem. Soc.* **2008**, 130, 3023.
- [36] Z. K. Heiba, L. Arda, Y. S. Hascicek, *J. Appl. Cryst.* **2005**, 38, 306.

- [37] M. R. Levy, C. R. Stanek, A. Chroneos, R. W. Grimes, *Sol. Stat. Sci.* **2007**, 9, 588.
- [38] C. Chang, Q. Zhang, D. Mao, *Nanotech.* **2006**, 17, 1981.
- [39] C. Chang, D. Mao, *Int. J. Chem. Kinetics* **2007**, 39, 75.
- [40] B. Antic, M. Mitric, D. Rodic, Y. Zhong, Y. Artemov, S. Bogdanovich, J. R. Friedman, *Phys. Rev. B* **1998**, 58, 3212.
- [41] R. M. Moon, W. C. Koehler, *Phys. Rev. B* **1975**, 11, 1609.
- [42] P. Dorenbos, *J. Lumin.* **2005**, 111, 89.
- [43] M. Buijs, A. Meyerink, G. Blasse, *J. Lumin.* **1987**, 37, 9.
- [44] R. B. Hunt, R. G. Pappalardo, *J. Lumin.* **1985**, 34, 133.
- [45] D. Ananias, S. Ferdov, F. A. A. Paz, R. A. S. Ferreira, A. Ferreira, C. F. G. C. Galdes, L. D. Carlos, Z. Lin, J. Rocha, *Chem. Mater.* **2008**, 20, 205.
- [46] T. Igarashi, M. Ihara, T. Kusunoki, K. Ohno, T. Isobe, M. Senna, *Appl. Phys. Lett.* **2000**, 76, 1549.
- [47] R. M. Rason, E. Evangelou, C. B. Thomas, *Appl. Phys. Lett.* **1998**, 72, 2663.
- [48] R. S. Meltzer, S. P. Feofilov, B. Tissue, H. B. Yuan, *Phys. Rev. B* **1999**, 60, R14012.